



Published in final edited form as:

Comput Med Imaging Graph. 2018 January ; 63: 41–51. doi:10.1016/j.compmedimag.2018.01.001.

An automated method for choroidal thickness measurement from Enhanced Depth Imaging Optical Coherence Tomography images

Md Akter Hussain^{a,*}, Alauddin Bhuiyan^b, Hiroshi Ishikawa^c, R. Theodore Smith^c, Joel S. Schuman^c, Ramamohanrao Kotagiri^a

^aDepartment of Computing and Information Systems, The University of Melbourne, Australia

^bNew York University, USA

^cOphthalmology, NYU School of Medicine, USA

Abstract

The choroid is vascular tissue located underneath the retina and supplies oxygen to the outer retina; any damage to this tissue can be a precursor to retinal diseases. This paper presents an automated method of choroidal segmentation from Enhanced Depth Imaging Optical Coherence Tomography (EDI-OCT) images. The Dijkstra shortest path algorithm is used to segment the choroid–sclera interface (CSI), the outermost border of the choroid. A novel intensity-normalisation technique that is based on the depth of the choroid is used to equalise the intensity of all non-vessel pixels in the choroid region. The outer boundary of choroidal vessel and CSI are determined approximately and incorporated to the edge weight of the CSI segmentation to choose optimal edge weights. This method is tested on 190 B-scans of 10 subjects against choroid thickness (CTh) results produced manually by two graders. For comparison, results obtained by two state-of-the-art automated methods and our proposed method are compared against the manual grading, and our proposed method performed the best. The mean root-mean-square error (RMSE) for finding the CSI boundary by our method is 7.71 ± 6.29 pixels, which is significantly lower than the RMSE for the two other state-of-the-art methods (36.17 ± 11.97 pixels and 44.19 ± 19.51 pixels). The correlation coefficient for our method is 0.76, and 0.41 and 0.66 for the other two state-of-the-art methods. The interclass correlation coefficients are 0.72, 0.43 and 0.56 respectively. Our method is highly accurate, robust, reliable and consistent. This identification can enable to quantify the biomarkers of the choroid in large scale study for assessing, monitoring disease progression as well as early detection of retinal diseases. Identification of the boundary can help to determine the loss or change of choroid, which can be used as features for the automatic determination of the stages of retinal diseases.

Keywords

Biomedical optical imaging; Image segmentation; Layer segmentation; Retina; Choroid; Shortest path problem; Enhanced Depth Imaging Optical Coherence; Tomography (EDI-OCT)

*Corresponding author. hussain@student.unimelb.edu.au (M.A. Hussain).

1. Introduction

Optical coherence tomography (OCT) is a non-invasive biomedical imaging technique that enables in vivo, high resolution, cross-sectional imaging of the retina and choroid using coherent Infrared light (Drexler and Fujimoto, 2008; Huang et al., 1991; Abramoff et al., 2010; Kanagasingam et al., 2014) that also enables three-dimensional (3D) reconstruction. The retinal image quality obtained from current OCT technology cannot be achieved by other currently available methods, giving it a comprehensive clinical application (Kaji et al., 2013; Albarrak et al., 2017). Currently, there are several types of OCT imaging available including Spectral Domain Optical Coherence Tomography (SD-OCT), Swept Source Optical Coherence Tomography (SSOCT) and Enhanced Depth Imaging Optical Coherence Tomography (EDI-OCT). In 2008, Spaide et al. modified existing SD-OCT technology to allow Enhanced Depth Imaging (EDI) of the retina and improved the visualisation of choroid (Spaide et al., 2008). The EDI method of SDOCT places a zero delay line on the choroid to obtain high-resolution cross-sectional images of the choroid, enabling quantitative measurement of choroid thickness and volume (Spaide et al., 2008; Margolis and Spaide, 2009; Spaide, 2009; Branchini et al., 2012; Chhablani et al., 2012; Shao et al., 2013). Fig. 1 shows an example of an EDI-OCT B-scan image of the human retina and choroid.

The choroid is a vascular plexus located between the retina and the sclera (Fig. 1). It provides oxygen and metabolic support to the retinal pigment epithelium (RPE), outer retina, and optic nerve and absorbs the excess light penetrating the retina (Margolis and Spaide, 2009; Nickla and Wallman, 2010). The retina has ten layers (Hussain et al., 2017). Fig. 1 depicts four prominent retinal layers, the choroid and sclera. We have used these retinal layers to map the choroid. Anatomically, the choroid can be divided into two major components: choroidal vessels and stroma (Hogan and Weddell, 2018). The choroidal vessels are further subdivided into three major layers of increasing size: Choriocapillaris, Sattler's and Haller's layers. The Choriocapillaris (Cc) is adjacent to Bruchs membrane and is comprised of small fenestrated capillaries, whereas the outer Sattler's and Haller's layers feed the Cc network. The choroidal stroma is comprised of melanocytes, fibroblasts, immune cells, neurons, and ground substance that contribute to its thickness (Nickla and Wallman, 2010). The choroidal vessels (CV) appear as the black regions surrounded by white pixels in the choroidal region of the EDI-OCT image. The Bruch's membrane (BM) is a semi-permeable membrane located between the Cc and the RPE. The BM and Cc are typically not distinguishable from the outer RPE except in pathologic state. Because of this, the term outer RPE-BM-Choriocapillaris complex (RBC) is typically used to demarcate the separation of the retina and choroid (Kaji et al., 2012).

The qualitative and quantitative evaluation of the choroid is important in the study of glaucoma (Yin et al., 1997), age-related macular degeneration (AMD) (Spaide, 2009), choroidal melanoma (Torres et al., 2011), central serous chorioretinopathy (Gemenetzi et al., 2010), and many other retinal and systemic diseases (Altinkaynak et al., 2014; Chen et al., 2015). Quigley (2009) proposed that a mere 50 μm choroidal expansion can increase the intraocular pressure to harmful levels in angle closure glaucoma patients. Some choroidal thinning occurs during normal aging, although, in some cases, a pathologic condition

referred to as age-related choroidal atrophy can occur (Spaide et al., 2008). There has also been an increasing interest in investigating the correlation of CTh with the age, gender, axial length and intra-ocular pressure in healthy human eyes (Ikuno et al., 2010; Ding et al., 2011; Manjunath et al., 2010). Since manual segmentation of CTh is time consuming, prone to error and significant inter- and intra-grader variability, many automatic segmentation attempts have been performed. Recent reports have demonstrated the automated measurement of CTh in healthy and pathologic states using optical coherence tomography (OCT) images (Spaide et al., 2008; Margolis and Spaide, 2009; Chen et al., 2015; Tanabe et al., 2012; Regatieri et al., 2012; Moreno et al., 2013). Approaches include active contour method (Yazdanpanah et al., 2009), intensity-based Markov boundary models (Koozekanani et al., 2001), graph theory and dynamic programming (Chiu et al., 2010; Gao et al., 2017; Miri et al., 2017), machine learning (Lang et al., 2013), and graph-based multi-surface segmentation with or without CSI detection (Garvin et al., 2009; Dufour et al., 2013). A detailed description of the existing methods are presented in Section 2. However, these methods have limitations for the unpredictable size of the choroid (Chen et al., 2015). The lack of robustness and accuracy of the automatic choroid detection (choroid is defined by the RBC and CSI boundaries) and the need of automatic algorithm for monitoring and diagnosis of choroidal diseases motivated us to develop a robust, reliable and more accurate automatic system for the measurement of CTh. In this paper, we have proposed to develop an automatic method for segmenting the Choroid Sclera Interface (CSI) and computing CTh from EDI-OCT images.

2. Background and motivation

A large number of studies have been reported semi-automatic and automatic methods of choroidal segmentation in OCT images (Chen et al., 2015; Kaji et al., 2012; Hu et al., 2013; Tian et al., 2013). These methods utilise machine learning, graph shortest path, min-cut-max-flow, eigenvector analysis, tensor matrix and Gaussian mixture model for finding the CSI and/or CV borders from different types of OCT images such as HD-OCT, PS-OCT, SD-OCT and EDI-OCT (Chen et al., 2015; Kaji et al., 2012; Hu et al., 2013; Tian et al., 2013; Torzicky et al., 2012). We have summarised these methods with the algorithms, accuracy and drawbacks in Table 1 where boundary is named by our naming convention for example outer RPE is RBC.

3. Proposed method

Fig. 2 shows the flow diagram for our proposed method. Three retinal reference layers (RNFL, ONL and RPE) have been identified first to map the choroidal region. Since the choroid is located under RBC boundary and the maximum thickness of the choroid is approximately 350 μm in healthy individuals (Manjunath et al., 2010), the region of interest (ROI) for the choroid is defined 400 μm underneath the RBC boundary. Depth-based intensity normalisation (DIN) methods are developed to achieve a continuous and stable pattern of intensity for CSI. Choroidal vessels (CV) are located approximately using Otsu's clustering method (Otsu, 1975). An anatomical knowledge-based probability map from the DIN image is generated to find the approximate CSI. Following that, the approximate outer choroidal vessels (OCV) boundary is detected using the approximate CV, approximate CSI

and convex hull. The steps for choroid detection and thickness measurement are described in the following subsections.

3.1. Segmenting ILM-RNFL & RBC

The ILM-RNFL and the RBC boundaries have been segmented using the Dijkstra's shortest path algorithm where edge weight is designed by boundary oriented parameter such as nodes association to a boundary (Hussain et al., 2017). The Wiener and Anisotropic Diffusion (AD) filters are used to reduce image noise without distorting the edge of boundaries. After detecting the ILM-RNFL boundary, the search space is reduced to find the RBC boundary, thus improving the accuracy and efficiency of its detection even in the presence of pathologies (Hussain et al., 2017). The edge pixels are detected using the Canny edge detection algorithm. Edge pixels with a positive gradient are considered candidate pixels for the ILM-RNFL boundary and those with a negative gradient are considered to be candidate pixels for the RBC boundary. Three reference layers (RNFL, ONL and RPE) are determined to find the region of interest for tracking the boundaries (Hussain et al., 2015a,b,2017). The approximate positions of these three reference layers are determined using their prior knowledge of relative intensities and relative positions. The contiguous candidate pixels in the ROI are split into small parts and each part is a pixel group. The end pixels of each pixel group form the graph nodes. The edge weights are determined using spatial distance, slope similarity to the relative reference boundary and layer associativity (measured by pixel's relevance of the corresponding layer) between the nodes. The Dijkstra's shortest path algorithm (Dijkstra, 1959) is used to define the boundary. Here we have explained the detection of these boundaries briefly which are explained in Hussain et al. (2017) in details.

3.1.1. Noise reduction—The Wiener Filter removes additive noise and inverts blurring simultaneously (Baraniuk, 1995). On the other hand, Anisotropic Diffusion (AD) (Perona and Malik, 1990) can successfully smooth noise while preserving the region boundaries and small structures within the image, a very essential feature for OCT B-scan image analysis. In our method, we have used Wiener filter twice with 3×15 and 3×17 windows, these window sizes were found using Simulated Annealing (SA), a probabilistic technique for approximating the global optimum. Since images have different resolution in the x and y -axis (that is, boundaries are horizontally expanded) we choose a rectangular window size to smooth the image and reduce noise. Following this, the AD filter is applied twice with $K = 32$, the numbers of first and second iteration are 8 and 3 which were determined using SA.

3.1.2. Discover approximate location of three reference (aprxTRL) layers—Three reference (TR) layers are used to select the ROI for ILM-RNFL and considered into feature computation, as shown in Fig. 3. These TR layers are retinal nerve fiber layer (RNFL), outer nuclear layer (ONL) and retinal pigment epithelium (RPE) layer. The TR layers are detected approximately by the prior knowledge of relative intensity and distance of the TR layers using (1) where indexes are used to maintain relative distance and intensity. As a result, index from (1) by finding maximum value in a highly Gaussian smoothed image will give a good approximate location of three reference (*aprxTRL*) layers (Hussain et al.,2017).

$$C_{m, rp, on} = \arg \min_{m, rp, on} (I_m + I_{rp} - I_{on}) \quad (1)$$

where the indexes m , rp , and on represent the position of RNFL, RPE and ONL layers respectively in the A-scan and I_x represents the intensity of image at position x where $x \in \{m, rp, on\}$. The image had been smoothed by a Gaussian filter.

3.1.3. Edge weight computation for the retinal boundary detection—We utilise three features to compute edge weights for the boundaries: spatial distance, slope similarity to a reference and pixel relevance to the boundary using (2). For computing spatial distance, slope similarity to a reference line and pixel relevance to the layer, we use (3)–(5), respectively, details will be found in (Hussain et al., 2017). The first order polynomial line on the approximate RNFL and RPE is used as the reference line for the identification of the ILM-RNFL and RBC boundaries respectively.

$$\omega_{a,b} = \phi_{a,b} + \psi_{a,b}^r + \gamma_{a,b} \quad (2)$$

where $\phi_{a,b}$ represents the spatial distance between pixels a and b , and is high when a and b are away from each other. This is defined by (3); $\psi_{a,b}^r$ represents slope between a and b relative to an already determined reference line (r), and is high when the slope is not similar to the reference. This is defined by (4); and $\gamma_{a,b}$ represents how well the pixel group containing b matches pre-defined properties of pixels forming the boundary, and is high when pixels do not conform to that property. This is defined by (5);

$$\phi_{a,b} = \begin{cases} 0 & , \text{ if } a = b \\ \alpha_0 & , \text{ if } a \text{ \& } b \text{ in the same pixel-group} \\ \alpha_1 |a_x - b_x|^2 + \\ \alpha_2 |a_y - b_y|^2 + & , \text{ otherwise} \\ \alpha_3 \left| \frac{a_y - b_y}{a_x - b_x} \right|^2 \end{cases} \quad (3)$$

where α_1 , α_2 , and α_3 are three parameters, and a_x , a_y , b_x and b_y are the coordinate position of nodes a and b . $\alpha_0 = 0.0001$ is found using SA.

$$\psi_{a,b}^r = |(r(a_x) - a_y) - (r(b_x) - b_y)| \quad (4)$$

where $r(x)$ is the y value of the reference boundary r at x -coordinate x .

$$\gamma_{a,b} = \sum_i (1 + E_b - f_{b,i})^{p_i} \quad (5)$$

where E_b is the number of pixels in the pixel-group containing node b , i is 1 to the total number of properties (properties are explained in the following paragraph), $f_{b,i}$ is the number of associated pixels for i th property in the pixel group containing node b , and p_i is a parameter to control the influence of each property.

The property of the layers to compute the $\gamma_{a,b}$. The layer associativity is computed using (5) where associated pixels are selected by considering layer property. Two properties are considered for the ILM-RNFL boundary detection and one property is considered for the RBC boundary. They are as follows. Properties of the ILM-RNFL boundary:

- The candidate pixels that are the closest and above the aprxRNFL layer along each A-scan with $p_1 = 2$.
- The candidate pixels above the aprxONL layer along A-scan with $p_2 = 2$.

Property of the RBC boundary:

- The candidate pixels that are closest and under the aprxRPE layer along each A-scan with $p_1 = 2$.

3.1.4. Boundary construction—After computing edge weight, the shortest path is computed using Dijkstra's shortest path algorithm. Start and end nodes are added automatically to compute the edge weight with other nodes by considering only the x-axis distance. The start and end nodes are removed in the reconstruction phase. The pixel group of the corresponding shortest path nodes are fetched and combined by extrapolation with a continuous line. Gaussian smoothing is applied to remove zigzags and to find a smooth line. Fig. 4 shows an example of ILM-RNFL and RBC segmentation. ILM-RNFL is delineated using a green line and RBC using a red line.

3.2. CSI boundary detection

The CSI boundary is determined by finding the region of interest, followed by noise reduction and intensity normalisation. To get a similar intensity for the surface of the choroid and sclera, depth-based intensity normalisation (DIN) is used. Choroidal vessel, the OCV and CSI are detected approximately to allow for more accurate detection of the CSI. Each pixel from the graph nodes and edge weight is computed using the normalised intensity and the approximate CSI and OCV boundary. Finally, shortest path defined the CSI boundary. The details of CSI detection are described below.

3.2.1. The ROI, noise reduction & normalization—Since the maximum thickness of the choroid is approximately 350 μm (Manjunath et al., 2010), the search space is defined a slightly to be more, 400 μm from the RBC boundary. The red to yellow line in Fig. 4 is selected as ROI and Fig. 5(a) shows the crop of the ROI.

The choroidal region contains many small vessels, creating edges that increase the difficulty of CSI detection. Noise can create additional false edges. The filters which are used to de-noise the image during the detection of the ILM-RNFL and RBC boundaries cannot resolve this type of noise. For this purpose, more smoothing operations are applied to reduce false edges, thus improving the accuracy of the identification of the CSI. Gaussian and Median filters are applied on the ROI in two steps. Before applying these filters, the intensities that are higher than a threshold due to imaging technology are replaced by that threshold using (6).

$$I(x, y) = \begin{cases} I(x, y), & \text{if } I(x, y) < th_x \\ th_x, & \text{if } I(x, y) \geq th_x \end{cases} \quad (6)$$

where th_x is the threshold value and $th_x = \mu(I_x) + 2 \times \sigma(I_x)$. $\mu(I_x)$ and $\sigma(I_x)$ are the mean intensity and standard deviation of the image I at x th A-scan. Following this step, a median filter of 5×5 window is applied. The intensity of the image is normalised to values in the range 0–1 for each A-scan. Gaussian filter with the window size of 5×5 and standard deviation of 1 is then applied to further smoothen the image (Fig. 5(b)).

3.2.2. Depth based intensity normalisation (DIN)—The intensities of the choroidal vessel and non-vessel pixels (referred to here as surface pixels) are not evenly distributed, and the intensity of the sclera region is similar to the choroidal vessel intensity (as shown in Fig. 5). The even distribution of the surface pixels of the choroid and sclera improved the identification of the CSI significantly. To allow for such normalisation, we propose a method that adapts the properties of the OCT image capturing technology to the anatomy of choroid and sclera. OCT imaging technology shows low intensity for the vessel and high intensity for the surface tissues. The intensity values also become lower as the depth increases. The goal of our proposed depth based normalisation method is to make the intensity of the surface pixels of the choroid and sclera stable and to make the intensity of the choroidal vessels pixels lower than the surface pixels. Since the pixel intensity decreases with the increasing of depth, we use the depth information to normalise the image for the CSI detection. This simple and efficient method represents a significant novel step in our proposed method. This DIN method is shown by (7).

$$N(x, y) = \frac{(\sum_k \sum_l I(x, y) > I(k, l))}{n} \quad (7)$$

where $I(x, y)$ is the intensity value of the pixel located at x th row and is y th column. $x = k$ #row and $y = l$. $n = |k| \times |l|$. $N(i, j)$ is the computed depth normalised intensity value.

The new intensity value of a pixel is the total number of lower intensity pixels located under that pixel. The value is divided by the number of pixels located under that pixel. This process uses multiple neighbour A-scans instead of single A-scan for the robustness of the method over noise which is formulated in (7) with $k=2$. This operation converts the surface pixels to a similar intensity. Fig. 5(c) shows an example of the output of the DIN process.

3.2.3. Choroidal Vessel (CV) approximation—The depth based intensity normalisation (DIN) technique helps to differentiate the surface and vessel pixels, where the higher intensities are the surface and the lower intensities are the vessels. The vessel and surface pixels vary widely in the DIN image. We note that, we want an approximate result instead of an exact detection in this phase. Therefore, we consider the first six out of seven clusters using the Otsu method for initial approximation of CV as shown in Fig. 6(a). To reduce false vessel pixels, two morphological operations (opening and closing) are applied to the initial approximation. The morphological opening operation removed noise based on

the size of the blob as shown in Fig. 6(b). The closing operation recovered deleted pixels from the border of the vessels for the opening operation as shown in Fig. 6(c). These operations are applied by a disk as a blob with a radius of 5.

The initial approximation of the CV could, at times, have the sclera region as shown in Fig. 6(c), represented by the white pixels in the lower part of the image. A dynamic distance filter is applied to the initial approximation for removing the sclera region as much as possible and output is shown in Fig. 6(d). This dynamic distance filter selects pixels as vessels based on the distance of the already classified vessel pixels along A-scan. At first, the top 200 μm initial approximated pixels are classified as approximated vessel pixels. If the distance between the classified pixels and next initial approximated pixels is less than a threshold value, then that next pixels are also classified as approximated vessel pixels and computation is continued iteratively until no pixels are found as approximated vessel pixels. That threshold value is defined dynamically based on the position of the current pixels. For example, suppose that the black pixels in Fig. 7(a) are the initial approximated vessel pixels. There are two A-scans and each A-scan has two pixels. The red colour pixels in Fig. 7(b) are classified as approximated pixels as they are located in the top 200 μm . The distances between two pixels in the A-scan are d_1 and d_2 where d_1 is less than the threshold value and d_2 is greater than the threshold value. Then the pixel located at d_1 is included in the approximated vessel but that at d_2 is not, as shown in Fig. 7(c). The threshold is defined dynamically based on the position of the pixels that is $\text{th}_{x,y}^d = 100/e^{x/400} \mu\text{m}$ where $\text{th}_{x,y}^d$ is the distance threshold for the pixel at x th row and y th A-scan or column.

3.2.4. Approximate detection of CSI and OCV—The approximations of the CSI and OCV are used to manipulate the edge weight of the graph for selecting pixels as shortest path that is more likely to be the CSI. The approximated CSI line is identified based on prior information from localising the CSI and surface pixels. The cluster having the highest intensity by the Otsu method at the approximation of the choroidal vessel location is classified as surface pixels, shown in Fig. 8(a). The approximated CSI is used to search 100 μm (i.e., approx. 25 pixels) away from the RBC. This explains why the pixels located in the top 100 μm are removed from the surface pixels as shown in Fig. 8(b). A probability matrix is computed based on the position of the pixels. The hypothesis behind computing the probability matrix is that the approximated CSI is more likely to be located near the maximum CTh (350 μm away from the RBC boundary). The probability value of a pixel decreases with the increasing distance from the position of the maximum CTh. This is formulated in (8) and shown in Fig. 8(c) in the means of intensity (high intensity means high probability and low intensity means low probability).

$$P(x, y) = \exp^{-|x - \hat{h}|/\eta} \quad (8)$$

where $P(x, y)$ is the probability value of a pixel located at the x th row and y th column, \hat{h} is the hypothesised position of the CSI boundary which is 350 μm and η is the normalised value which is set to 200 μm empirically.

After computing the probability matrix, the next step is to find the approximated CSI line. The pixels having maximum probability value in each A-scan are selected as candidate

pixels (red pixels in Fig. 8(d) for CSI). A first order polynomial line is fitted (green line in Fig. 8(e)) along these candidate pixels. Then the candidate pixels located under that fitted line by more than a threshold along A-scan are removed and their probability values are changed to zero so that they are not selected for the next iteration (magenta colour pixels in Fig. 8(f)). The threshold value is defined by the standard deviation of the distance between fitted line and candidate pixels under that fitted line. This procedure is applied iteratively until no pixels are found to remove. When the product of threshold value and the number of pixels removed is at a minimum, the first order polynomial fitted line on the candidate pixels at that iteration became the approximated CSI. Fig. 9 shows an example of (a) the depth normalised image, (b) approximated vessel, (c) approximated CSI (green line) in the surface image (white colour).

After finding the approximated CSI line, approximated vessel pixels located under that approximated CSI line are removed to find a convex hull for the remaining pixels. The outer boundary of the convex hull is smoothed using average filter with window size of one fifth of the image width. This smooth line is defined as the OCV boundary. Fig. 9(d) shows an example of the approximated OCV boundary (red line) and vessels (white colour pixels). Fig. 9(e) shows the example of the approximated CSI (green line) and OCV boundary (red line) on the normalised image. The proposed method boosts the priority of those pixels located in between the approximated CSI and OCV for becoming the actual CSI by incorporating the edge weight computation.

3.2.5. Edge weight computation—The CSI detection problem is modelled as a graph shortest path problem where each pixel is the graph node. The nodes are connected with 8 neighbours. The vertex weight is computed using (10) with the intensity of the smooth image and intensity and gradient of the DIN image. The approximated CSI and outer vessel boundary also incorporated with the weight computation as a distance factor. The weight of the nodes is decreased with increasing distance from the any of the boundaries. The distance factor of the approximate CSI and approximate choroidal vessel outer boundary from the pixels are computed using (9).

$$df_{x,y}^{\lambda} = \alpha \times \exp\left(-\frac{(\lambda_y - x)^{\beta}}{\delta}\right) \quad (9)$$

where $df_{x,y}^{\lambda}$ is the distance factor of a node at the x th row and y th column for the reference line (λ). λ_y gives the position of the row for the y th column of λ . α , β and δ are three coefficients to manipulate the equation as follows. The approximated CSI and outer boundary of choroidal vessel are used as r in (9). The coefficient values in (9) for approximated CSI (df^{CS}) are $\alpha = 0.25$, $\beta = 1$ and $\delta = 100$. The coefficient value in (9) for approximated outer boundary of choroidal vessel (df^{OCV}) are assigned empirically and they are $\alpha = 0.5$, $\beta = 1$ and $\delta = 100$.

The DIN image is normalised in the range 0–1 for each A-scan. The vertex weight for the node is computed using the normalised intensity of the DIN image, gradient of that

normalised value, distance factor for the approximated CSI and outer choroidal vessel boundary. This computation of the vertex weight is formulated by (10).

$$V = \exp\left(-\left(N_{\text{DIN}} + G_{\text{DIN}}\right) \times \left(\text{df}^{\text{CSI}} + \text{df}^{\text{OCV}}\right) + 1\right) \times \left(I_s \times \text{df}^{\text{pcsi}}\right) \quad (10)$$

where N_{DIN} and G_{DIN} are the depth normalised intensity and its vertical gradient value respectively, df^{CS} and df^{OCV} are the distance factor of the approximated CSI and OCV respectively. I_s is the normalised image 0–1 of the after applying Gaussian and median filter image and df^{pcsi} is the distance factor for normalise intensity of the image for increasing intensity near CSI boundary and decreasing the intensity of the pixel located away from CSI. This helps the method to detect higher intensity pixels as CSI and at the same time, avoiding pixels near the RBC that are generally higher in intensity. df^{pcsi} is computed using (9) where λ is defined by the $(3 \times \text{aprxOCV} + \text{aprxCSI})/4$, $\alpha = 0.25$, $\beta = 2$ and $\delta = 1000$. aprxOCV is the approximated OCV and aprxCSI is the approximated CSI.

The first and last column pixels are set to a predefined minimum cost so that the shortest path algorithm could choose the first and last vertical position freely or independently as the starting and ending of the boundary. This predefined minimum value is set to 0.001. The edge weight of the graph is computed by (11). Then the shortest path algorithm is applied where the start node is left top pixels, and the destination node is the bottom right node.

$$W_{u,v} = V_v \quad (11)$$

where $W_{u,v}$ is the edge weight between node u and v , V_v is the vertex weight of node v that is computed by (11); u and v must be 8-connected neighbour.

The computed shortest path is formed to be the CSI. An average low-pass smoothing filter window size of one fifth of the width of b-scan image is applied on this shortest path for a smooth line instead of any zigzag line. This smooth line defined the CSI. Fig. 10 shows (a) original image as a reference, (b) segmented output of the ILM-RNFL (green line), RBC (red line) and CSI (yellow line) by our proposed method.

3.3. Choroidal vessel (CV) detection

After detecting the CSI, it can still be challenging to find the CV boundaries due to unstable shape and intensity distribution. Our proposed DIN method increases the accuracy of CV detection and increases efficiency. We have used the active contour method for detecting the CV boundaries where seed point is generated by applying clustering on the DIN image. The ROI for the CV boundary detection is the choroidal region that is from the RBC boundary to CSI. First, ROI in the DIN image is clustered into two regions by Otsu method. The cluster with the lowest intensity defined the initial CV that serves as the seed points of the active contour. Following that, due to uneven intensity distribution of the image, we divide the ROI into five parts along the width of the image. For each part, edge-based active contour is used to finalise the vessel area. The active contour is used from Matlab library function where it is iterated 300 times. Smooth factor and contraction bias are defined empirically by 0.1 and 0.01 respectively. Fig. 10(c) shows a segmented output of the CV boundaries.

4. Validation method

Validation is an important step for any automated method because to assess the accuracy and usability of the method. We compared our method against the manually segmented images (ground truth) and two state-of-the-art methods (Chen et al., 2015; Tian et al., 2013). Our assessment involves (1) direct evaluation of the precision of the boundary locations by computing: the root mean square error (RMSE) between two different segmentations; (2) dice coefficient (DC) between two different segmentations for direct evaluation of the precision of the overlap of the choroidal border; (3) root mean square error (RMSE) between two different segmentations for direct evaluation of the precision of the CTh measurement; (4) Pearson correlation coefficient and interclass correlation coefficient (ICC) for the choroid thickness between two different segmentation method. The performances of two automatic methods are reported using these four assessment methods to justify the accuracy and robustness of the method. The importance and computation process of the four evaluation protocols are described below.

4.1. Root mean square error (RMSE)

RMSE is the average pixel distance of a single boundary between two different segmentations. It is well known and the most often reported way to compare segmentation of objects or boundaries by different methods. A lower RMSE error means better accuracy or performance for the method. The formula of computing the RMSE is (12).

$$\text{RMSE}(B^{i,j_1}, B^{i,j_2}) = \sqrt{\frac{\sum_x (B^{i,j_1}(x) - B^{i,j_2}(x))^2}{\|A - \text{scan}\|}} \quad (12)$$

where B^{i,j_1} is the i th boundary by the j_1 method, $B^{i,j_1}(x)$ is the y -axis position of the i th boundary at x th A-scan by the method j_1 , $\|A - \text{scan}\|$ is the total number of A-scans, and x is taken over all A-scans.

4.2. Dice coefficient

This is a region-oriented analysis which provides more information about classification or identification errors. This allows us to assess whether the automatically delineated layer is more prone to under-segmentation or over-segmentation in comparison to manual segmentation. The dice coefficient (DC) is sensitive to variations in shape, size and position. The formula for DC is shown in (13) where i refers to a region, j_1 and j_2 refer to two methods of segmentation that they detect i th region.

$$\text{DC}(\text{Reg}^{(i,j_1)}, \text{Reg}^{(i,j_2)}) = \frac{2|\text{Reg}^{(i,j_1)} \cap \text{Reg}^{(i,j_2)}|}{|\text{Reg}^{(i,j_1)}| + |\text{Reg}^{(i,j_2)}|} \quad (13)$$

4.3. Interclass correlation (ICC)

ICC, also known as reliability coefficient, is an excellent parameter to evaluate an automatic method. A high-reliability coefficient of an automatic method represents high accuracy.

Shrout and Fleiss (1979) proposed a method to compute reliability coefficient called interclass correlation (ICC). Researchers have proposed six cases and our evaluation criteria are best satisfied by the third case, in which n targets are graded by k methods without any averaging. In this case, they proposed the ICC as follows.

$$ICC = \frac{BMS - EMS}{BMS + (k - 1) \times EMS} \quad (14)$$

where BMS is a between-targets mean square; EMS is a residual sum of squares. Let d is the data of $k \times n$ that is the ratings of n targets by k graders are stored in d . Then, BMS and EMS are computed by the following equations.

$$BMS = \frac{k \times \sum_i (\bar{d}_i - \bar{d})^2}{n - 1} \quad (15)$$

$$EMS = \frac{\sum_j \sum_i (d_{i,j} - \bar{d}_i)^2 - n \times \sum_j (\bar{d}_j - \bar{d})^2}{(k - 1) \times (n - 1)} \quad (16)$$

where \bar{d} is the mean of the ratings of all graders, \bar{d}_i is the mean of the ratings of the i th target by all graders, \bar{d}_j is the mean of the ratings of all targets by the j th grader and d_{ij} is the rating of the i th target by the j th grader.

5. Experimental setup

Our experimental setup consisted with 10 macular EDI-OCT volumes which are taken from 7 patients (each volume has 19 B-scan, Total 190 B-scans). All patients are imaged using EDI-OCT imaging on Heidelberg Spectralis HRA+OCT. Data is taken from patients without a history of retinal diseases seen at a large city hospital (average age 53 years, range 43–62). Each volume has $1021 \times 361 \times 19$ voxels with $3.9 \mu\text{m}$ axial resolution and dB (image quality parameter) ranges are 20–39. Two expert graders from our institution manually traced the RBC and CSI boundaries using Photoshop CS3. In addition, images are run through CTh measurement software developed by Tian et al. (2013) and Chen et al. (2015) to allow for comparison of their methods to ours. Each of the three automatic methods is compared to the results of the two manual graders and their average. We used several methods to compare the performance of the three systems, including RMSE to compute error for the RBC, CSI and CTh, DC for the choroidal region, and correlation coefficient and interclass correlation coefficient for the CTh. We have also shown the dice coefficient for each volume for different signal strength in dB (see Fig. 11). We have also collected two random SS-OCT B-scans from TEMBV (2016) to show the robustness of our proposed method in diseased eye and different source of OCT imaging. The parameter of the equations for the CSI detection is listed in Table 2.

6. Results

Our results show better accuracy compare to the state-of-the-art automatic methods (Chen et al., 2015; Tian et al., 2013). RMSE for the two boundaries RBC and CSI are reported in

Table 3. For the RBC boundary, our proposed method shows less error than other two state-of-the-art methods and inter-grader variability. The RMSE for the CSI shows that our proposed method is superior to the other automatic methods. Though our proposed method has a higher error than inter-grader variability, this difference is very small, as reported in Table 3. Our method has a DC of more than 92% where other two automatic methods have less than 65% and 70%. The RMSE, correlation coefficient (r) and interclass coefficient for the CTh also show our proposed method is superior to the methods of Tian et al. and Chen et al. The correlation coefficient (r) is more than 0.70 for our method but less than 0.51 for Tian et al. and less than 0.70 for Chen et al. The interclass correlation coefficient is 0.65 for our proposed method, and less than 0.45 and 0.60 for Tian et al. and Chen et al. respectively.

In Fig. 11, we have shown dice coefficient of each volume where x -axis represent dB value of the volume and y -axis represents the dice coefficient of the image. The dice coefficient from second manual grader, Tian et al., Chen et al. and our proposed method are shown in the Fig. 11 where the grading of first manual grader is used as gold standard. This figure shows the dice coefficient of our proposed method is very near to inter grade compared to other automatic methods. It is also clear that our method performs consistently in different signal strength.

Two B-scans from SS-OCT have been used to evaluate the performance of our proposed method in different OCT type and pathology existed eyes as shown in Fig. 12. In Fig. 12, (a) contains haemorrhage pathology from an AMD patient and (b) is from neovascularisation patient. Green, red and yellow line represent the ILM-RNFL, RBC and CSI respectively.

7. Novelty of the proposed segmentation algorithm for detecting the Choroid–Sclera Interface

Our proposed segmentation method for the detection of the CSI has the following novel features that help in finding CSI very accurately.

- Depth based intensity normalisation technique: The choroid is the noisiest area in the OCT image due to imaging technology and its anatomy. OCT technology is based on backscatter light from the tissues. As a result, it is sensitive to the depth of the tissue and loses sensitivity when increasing the depth of the tissue. Since the choroid is located under the retina, OCT cannot capture it with as high quality as the retina, although EDI-OCT and SS-OCT improve the quality of the image for the choroid. The images show high inconsistency in intensity even in the homogeneous area. The non-vessel regions of the choroid show high inconsistency in the intensity and it is worse under the large choroidal vessel where the CSI boundary is located. Moreover, the presence of the large choroidal vessel increases such challenges as it has non-uniform distribution and shape. To solve this intensity variation and inconsistency, we have proposed a novel depth-based intensity normalisation technique which helps to make this uneven intensity distribution to even out the homogeneous area of the choroid and the sclera region.

- Computation of edge weight: The second novelty in proposing the CSI detection is a robust method of computing edge weight where the approximate position of the CSI and other structural information such as the outer boundary of the choroidal vessel are incorporated. Use of the normalised image and its intensity gradient in the edge weight computation instead of the original image has also improved the accuracy of the method in detecting the CSI due to reducing inconsistency of the intensities in the choroid. The combination of all these operations makes our method robust and accurate and outperforms the state-of-the-art methods.

8. Conclusion

We have proposed an automated, robust and highly accurate method for the detection of the CSI. We evaluate our method on the EDI-OCT images with different signal to noise ratio which has shown similar accuracy when compared with grader. We have also shown the robustness of our proposed method by showing segmentation output in the SS-OCT B-scans with pathologies. We have incorporated a method for the detection of the ILM-RNFL and RBC from (Hussain et al., 2017) which is robust in the pathology existed images. Our proposed method, which is simple and novel, is a depth-based intensity normalisation (DIN) method for analysing CTh in EDI-OCT image technology. The normalisation method reduces the challenges of low contrast and unstable or unpredictable changes of the choroid layer by converting high distorted intensity values to a stable for the surface and vessel pixels of the choroid and sclera. This approach provide a high robustness in the low contrast choroid. Then the Dijkstra shortest path algorithm has been applied to detect robustly the CSI where the edge-weights are chosen based on two approximate boundaries, the OCV and CSI. The edge weights has helped to detect the accurate boundary in a noisy and low-contrast image by reducing the search space and increasing the value of the probability of the pixels which are more likely to be the CSI. We have shown our method to be far superior to the state- of-theart methods which has been established using several statistical tests including RMSE, DC and correlation coefficient. Our method has shown a performance similar to manual segmentation based on the inter-grader variability. The method of detecting ILM-RNFL and RBC has performed well even in the presence of pathology (Hussain et al., 2017) and here CSI detection method has performed well in the low-contrast and uneven thickness of the Choroid. Thus, the proposed method can be deployed for large-scale studies for tracking the progression and diagnosis of pathologies related to the choroid.

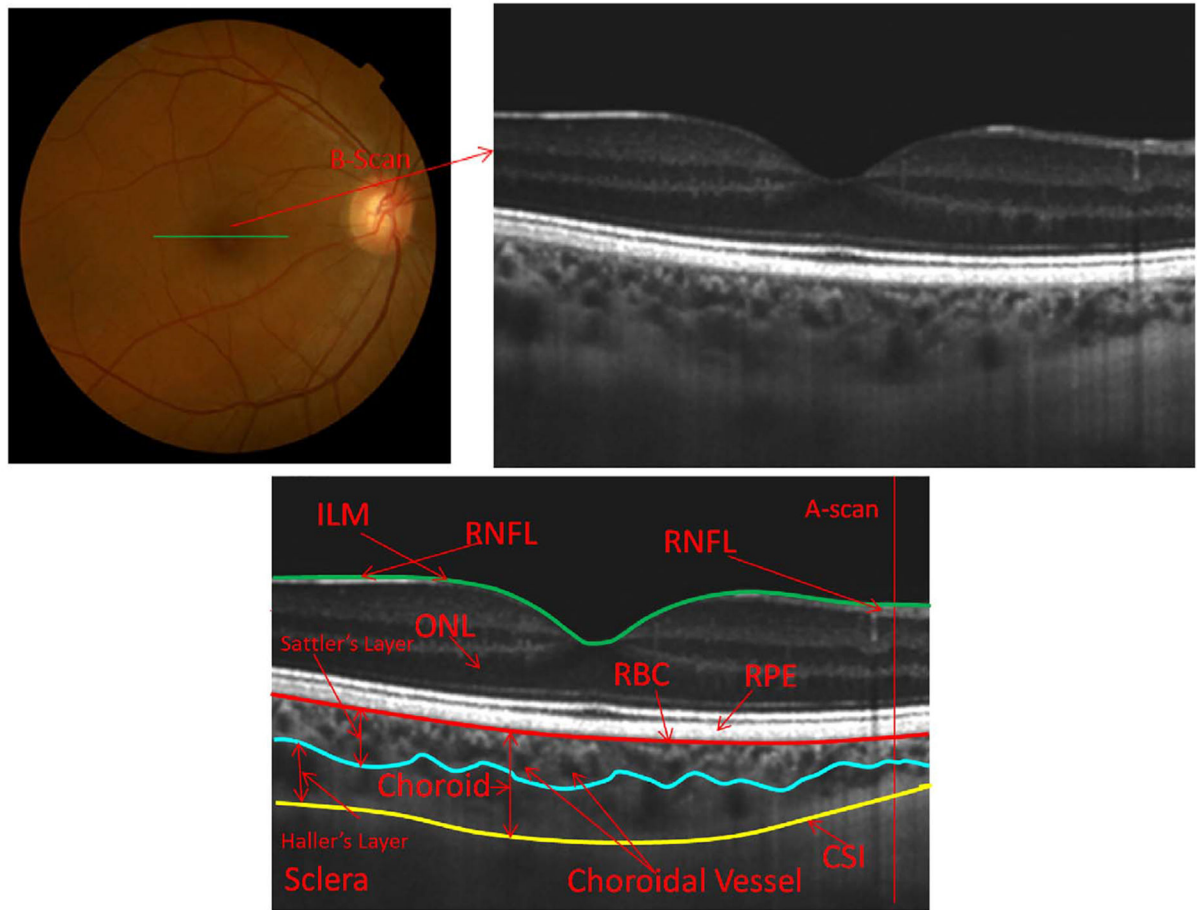
References

- Abràmoff MD, Garvin MK, Sonka M, 2010 Retinal imaging and image analysis. *IEEE Rev. Biomed. Eng* 3, 169–208. [PubMed: 22275207]
- Albarrak A, Coenen F, Zheng Y, 2017 Volumetric image classification using homogeneous decomposition and dictionary learning: a study using retinal optical coherence tomography for detecting age-related macular degeneration. *Comput. Med. Imaging Graph* 55, 113–123. [PubMed: 27507326]
- Alonso-Caneiro D, Read SA, Collins MJ, 2013 Automatic segmentation of choroidal thickness in optical coherence tomography. *Biomed. Opt. Express* 4 (12), 2795–2812. [PubMed: 24409381]

- Altinkaynak H, Kara N, Sayın N, Güne H, Av ar , Yazıcı AT, 2014 Subfoveal choroidal thickness in patients with chronic heart failure analyzed by spectral-domain optical coherence tomography. *Curr. Eye Res* 39 (11), 1123–1128. [PubMed: 24749809]
- Baraniuk RG, 1995 Wiener Filtering. <http://www.owl.net.rice.edu/elec539/Projects99/BACH/proj2/wiener.html>.
- Branchini L, Regatieri CV, Flores-Moreno I, Baumann B, Fujimoto JG, Duker JS, 2012 Reproducibility of choroidal thickness measurements across three spectral domain optical coherence tomography systems. *Ophthalmology* 119 (1), 119–123. [PubMed: 21943786]
- Chen Q, Fan W, Niu S, Shi J, Shen H, Yuan S, 2015 Automated choroid segmentation based on gradual intensity distance in HD-OCT images. *Opt. Express* 23 (7), 8974–8994. [PubMed: 25968734]
- Chhablani J, Barteselli G, Wang H, El-Emam S, Kozak I, Doede AL, Bartsch D-U, Cheng L, Freeman WR, 2012 Repeatability and reproducibility of manual choroidal volume measurements using enhanced depth imaging optical coherence tomography manual choroidal volume measurement using SD-OCT. *Investig. Ophthalmol. Vis. Sci* 53 (4), 2274–2280. [PubMed: 22427584]
- Chiu SJ, Li XT, Nicholas P, Toth CA, Izatt JA, Farsiu S, 2010 Automatic segmentation of seven retinal layers in SDOCT images congruent with expert manual segmentation. *Optics express* 18 (18), 19413–19428. [PubMed: 20940837]
- Danesh H, Kafieh R, Rabbani H, Hajizadeh F, 2014 Segmentation of choroidal boundary in enhanced depth imaging OCTs using a multiresolution texture based modeling in graph cuts. *Comput. Math. Methods Med*
- Dijkstra EW, 1959 A note on two problems in connexion with graphs. *Numerische mathematik* 1 (1), 269–271.
- Ding X, Li J, Zeng J, Ma W, Liu R, Li T, Yu S, Tang S, 2011 Choroidal thickness in healthy Chinese subjects. *Investig. Ophthalmol. Vis. Sci* 52 (13), 9555–9560. [PubMed: 22058342]
- Drexler W, Fujimoto JG, 2008 *Optical Coherence Tomography: Technology and Applications*. Springer Science & Business Media.
- Duan L, Yamanari M, Yasuno Y, 2012 Automated phase retardation oriented segmentation of choriocleral interface by polarization sensitive optical coherence tomography. *Opt. Express* 20 (3), 3353–3366. [PubMed: 22330573]
- Dufour PA, Ceklic L, Abdillahi H, Schroder S, De Dzanet S, Wolf-Schnurrbusch U, Kowal J, 2013 Graph-based multi-surface segmentation of OCT data using trained hard and soft constraints. *IEEE Trans. Med. Imaging* 32 (3), 531–543. [PubMed: 23086520]
- Gao Z, Bu W, Zheng Y, Wu X, 2017 Automated layer segmentation of macular OCT images via graph-based slic superpixels and manifold ranking approach. *Comput. Med. Imaging Graph* 55, 42–53. [PubMed: 27614678]
- Garvin MK, Abràmoff MD, Wu X, Russell SR, Burns TL, Sonka M, 2009 Automated 3-d intraretinal layer segmentation of macular spectral-domain optical coherence tomography images. *IEEE Trans. Med. Imaging* 28 (9), 1436–1447. [PubMed: 19278927]
- Gemenetzi M, De Salvo G, Lotery A, 2010 Central serous chorioretinopathy: an update on pathogenesis and treatment. *Eye* 24 (12), 1743–1756. [PubMed: 20930852]
- Hogan MJ, Weddell JJA, 2018 *Histology of the Human Eye: An Atlas and Textbook*.
- Hu Z, Wu X, Ouyang Y, Ouyang Y, Sadda SR, 2013 Semiautomated segmentation of the choroid in spectral-domain optical coherence tomography volume scans semiautomated choroid segmentation in SD-OCT. *Investig. Ophthalmol. Vis. Sci* 54 (3), 1722–1729. [PubMed: 23349432]
- Huang D, Swanson EA, Lin CP, Schuman JS, Stinson WG, Chang W, Hee MR, Flotte T, Gregory K, Puliafito CA, et al., 1991 Optical coherence tomography. *Science* 254 (5035), 1178–1181. [PubMed: 1957169]
- Hussain MA, Bhuiyan A, Ramamohanarao K, 2015a Automatic retinal minimum distance band (MDB) computation from SD-OCT images 2015 International Conference on Digital Image Computing: Techniques and Applications (DICTA), IEEE 1–8.
- Hussain MA, Bhuiyan A, Ramamohanarao K, 2015b Disc segmentation and BMOMRW measurement from SD-OCT image using graph search and tracing of three bench mark reference layers of retina Image Processing (ICIP), 2015 IEEE International Conference on, IEEE 4087–4091.

- Hussain MA, Bhuiyan A, Turpin A, Luu CD, Smith RT, Guymer RH, Kotagiri R, 2017 Automatic identification of pathology distorted retinal layer boundaries using SD-OCT imaging. *IEEE Trans. Biomed. Eng*
- Ikuno Y, Kawaguchi K, Nouchi T, Yasuno Y, 2010 Choroidal thickness in healthy Japanese subjects. *Investig. Ophthalmol. Vis. Sci* 51 (4), 2173–2176. [PubMed: 19892874]
- Kaji V, Esmaelpour M, Považay B, Marshall D, Rosin PL, Drexler W, 2012 Automated choroidal segmentation of 1060 nm OCT in healthy and pathologic eyes using a statistical model. *Biomed. Opt. Express* 3 (1), 86–103. [PubMed: 22254171]
- Kaji V, Esmaelpour M, Glittenberg C, Kraus MF, Honegger J, Othara R, Binder S, Fujimoto JG, Drexler W, 2013 Automated three-dimensional choroidal vessel segmentation of 3d 1060 nm OCT retinal data. *Biomed. Opt. Express* 4 (1), 134–150. [PubMed: 23304653]
- Kanagasigam Y, Bhuiyan A, Abramoff MD, Smith RT, Goldschmidt L, Wong TY, 2014 Progress on retinal image analysis for age related macular degeneration. *Prog. Retin. Eye Res* 38, 20–42. [PubMed: 24211245]
- Koozekanani D, Boyer K, Roberts C, 2001 Retinal thickness measurements from optical coherence tomography using a Markov boundary model. *IEEE Trans. Med. Imaging* 20 (9), 900–916. [PubMed: 11585207]
- Lang A, Carass A, Hauser M, Sotirchos ES, Calabresi PA, Ying HS, Prince JL, 2013 Retinal layer segmentation of macular OCT images using boundary classification. *Biomedical optics express* 4 (7), 1133–1152. [PubMed: 23847738]
- Manjunath V, Taha M, Fujimoto JG, Duker JS, 2010 Choroidal thickness in normal eyes measured using cirrus HD optical coherence tomography. *Am. J. Ophthalmol* 150 (3), 325–329. [PubMed: 20591395]
- Margolis R, Spaide RF, 2009 A pilot study of enhanced depth imaging optical coherence tomography of the choroid in normal eyes. *Am. J. Ophthalmol* 147 (5), 811–815. [PubMed: 19232559]
- Miri MS, Robles VA, Abramoff MD, Kwon YH, Garvin MK, 2017 Incorporation of gradient vector flow field in a multimodal graph-theoretic approach for segmenting the internal limiting membrane from glaucomatous optic nerve head-centered SD-OCT volumes. *Comput. Med. Imaging Graph* 55, 87–94. [PubMed: 27507325]
- Moreno TA, O'Connell RV, Chiu SJ, Farsiu S, Cabrera MT, Maldonado RS, Tran-Viet D, Freedman SF, Wallace DK, Toth CA, 2013 Choroid development and feasibility of choroidal imaging in the preterm and term infants utilizing SD-OCT choroid development and imaging feasibility. *Investig. Ophthalmol. Vis. Sci* 54 (6), 4140–4147. [PubMed: 23652488]
- Nickla DL, Wallman J, 2010 The multifunctional choroid. *Prog. Retin. Eye Res* 29 (2), 144–168. [PubMed: 20044062]
- Otsu N, 1975 A threshold selection method from gray-level histograms. *Automatica* 11 (285–296), 23–27.
- Perona P, Malik J, 1990 Scale-space and edge detection using anisotropic diffusion. *IEEE Trans. Pattern Anal. Mach. Intell* 12 (7), 629–639.
- Quigley HA, 2009 What's the choroid got to do with angle closure? *Archiv. Ophthalmol* 127 (5), 693–694.
- Regatieri CV, Branchini L, Fujimoto JG, Duker JS, 2012 Choroidal imaging using spectral-domain optical coherence tomography. *Retina (Philadelphia, Pa)* 32 (5), 865.
- Shao L, Xu L, Chen CX, Yang LH, Du KF, Wang S, Zhou JQ, Wang YX, You QS, Jonas JB, et al., 2013 Reproducibility of subfoveal choroidal thickness measurements with enhanced depth imaging by spectral-domain optical coherence tomography reproducibility of choroidal thickness measurement. *Investig. Ophthalmol. Vis. Sci* 54 (1), 230–233. [PubMed: 23060144]
- Shrout PE, Fleiss JL, 1979 Intraclass correlations: uses in assessing rater reliability. *Psychol. Bull.* 86 (2), 420.
- Spaide RF, Koizumi H, Pozonni MC, 2008 Enhanced depth imaging spectral-domain optical coherence tomography. *Am J. Ophthalmol* 146 (4), 496–500. [PubMed: 18639219]
- Spaide RF, 2009 Age-related choroidal atrophy. *Am. J. Ophthalmol* 147 (5), 801–810. [PubMed: 19232561]

- Tanabe H, Ito Y, Terasaki H, 2012 Choroid is thinner in inferior region of optic disks of normal eyes. *Retina* 32 (1), 134–139. [PubMed: 22080906]
- TEMBV, 2016 Topcon DRI OCT triton, swept source OCT. <http://www.sweptsourceoct.eu/images.html>.
- Tian J, Marziliano P, Baskaran M, Tun TA, Aung T, 2013 Automatic segmentation of the choroid in enhanced depth imaging optical coherence tomography images. *Biomed. Opt. Express* 4 (3), 397–411. [PubMed: 23504041]
- Torres VL, Brugnoli N, Kaiser PK, Singh AD, 2011 Optical coherence tomography enhanced depth imaging of choroidal tumors. *Am. J. Ophthalmol* 151 (4), 586–593. [PubMed: 21257150]
- Torzicky T, Pircher M, Zotter S, Bonesi M, Götzinger E, Hitzenberger CK, 2012 Automated measurement of choroidal thickness in the human eye by polarization sensitive optical coherence tomography. *Opt. Express* 20 (7), 7564–7574. [PubMed: 22453435]
- Vupparaboina KK, Nizampatnam S, Chhablani J, Richhariya A, Jana S, 2015 Automated estimation of choroidal thickness distribution and volume based on OCT images of posterior visual section. *Comput. Med. Imaging Graph* 46, 315–327. [PubMed: 26526231]
- Yazdanpanah A, Hamarneh G, Smith B, Sarunic M, 2009 Intra-retinal Layer Segmentation in Optical Coherence Tomography Using an Active Contour Approach In: *International Conference on Medical Image Computing and Computer-Assisted Intervention*. Springer pp. 649–656.
- Yin ZQ, Millar TJ, Beaumont P, Sarks S, et al., 1997 Widespread choroidal insufficiency in primary open-angle glaucoma. *J. Glaucoma* 6 (1), 23–32. [PubMed: 9075077]
- Zhang L, Lee K, Niemeijer M, Mullins RF, Sonka M, Abramoff MD, 2012 Automated segmentation of the choroid from clinical SD-OCT automated segmentation of choroid from SD-OCT. *Investigative ophthalmology & visual science* 53 (12), 7510–7519. [PubMed: 23060139]



Retinal Layers: **ILM:** Internal Limiting Membrane; **RNFL:** Retinal Nerve Fiber Layer; **ONL:** Outer Nuclear Layer; **RPE:** Retinal pigment epithelium.

RBC: The outer border of the RPE/ Bruch's membrane (BM)/ Choriocapillaris Complex; **CSI:** Choroid Sclera Interface

Fig. 1.

Colour fundus photograph image (left) and EDI-OCT image (middle) in a healthy eye. B-scan mode is demonstrated by the cross sectional image corresponding to the green line (left); A-scan mode is represented by red vertical line (right).

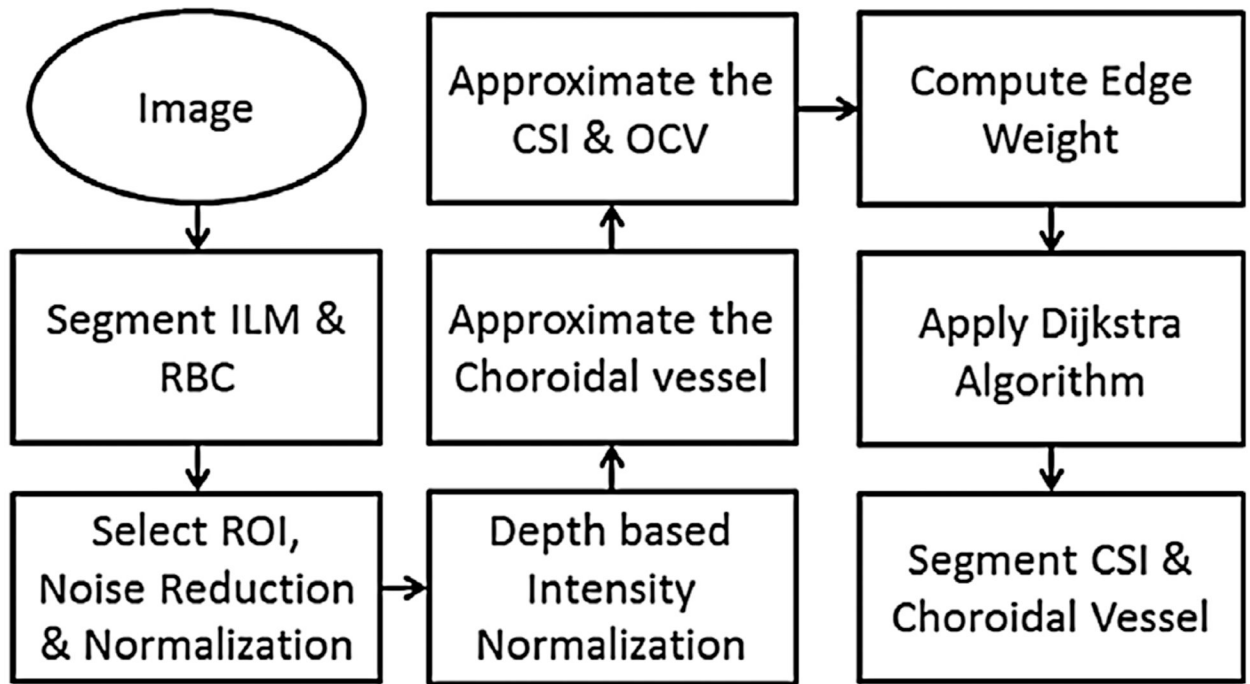


Fig. 2.
Flow diagram of the proposed method.

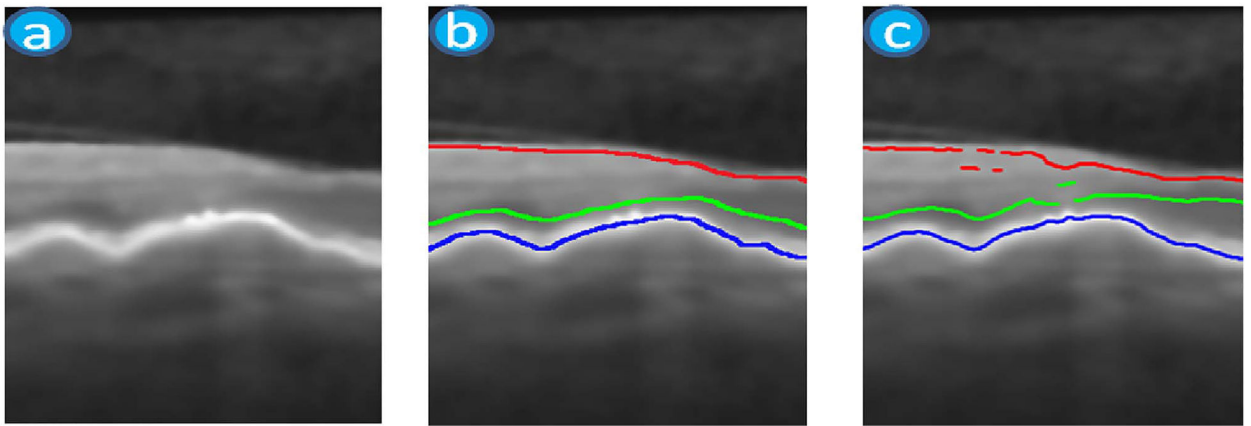


Fig. 3.

The TR layers' approximate detection: (a) is a smooth and a cropped portion of the retinal OCT B-Scan; (b) manually delineated TR layers; and (c) automatically discovered *aprxTRL* layers by our proposed method (red, green and blue lines represent the RNFL, ONL and RPE layer locations respectively). RNFL: retinal nerve fiber layer; ONL: outer nuclear layer; RPE: retinal pigment epithelium.

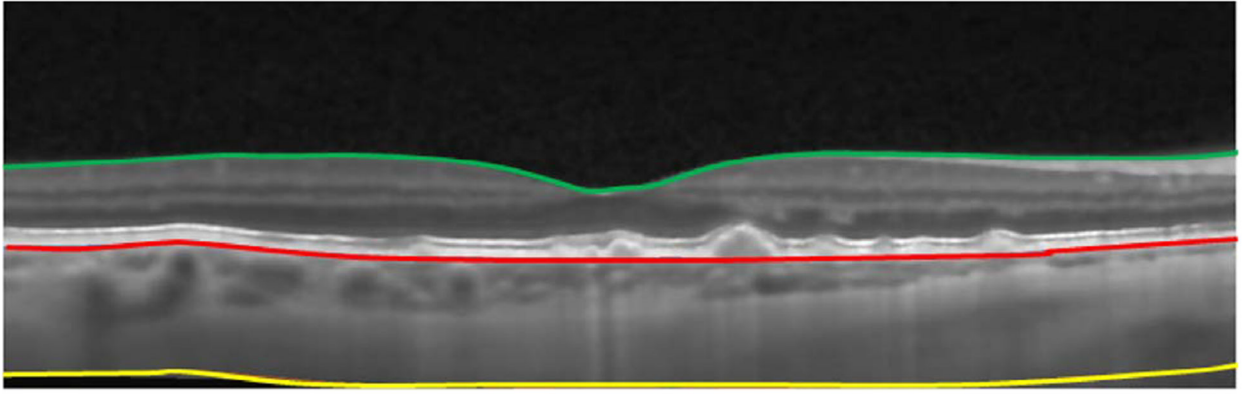


Fig. 4. Segmented result of ILM-RNFL (green line) and RBC (red line); The yellow line define the end of the region of interest for the choroid.

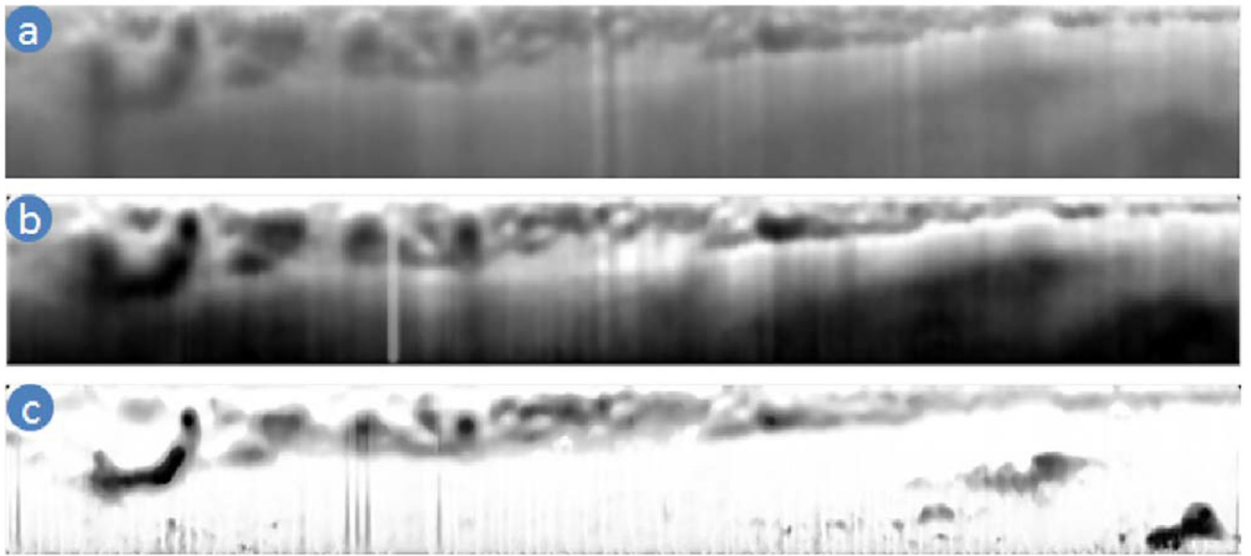


Fig. 5.
(a) The region of interest of the choroid, (b) the smooth image after intensity normalisation and (c) depth-based intensity normalised (DIN) image.

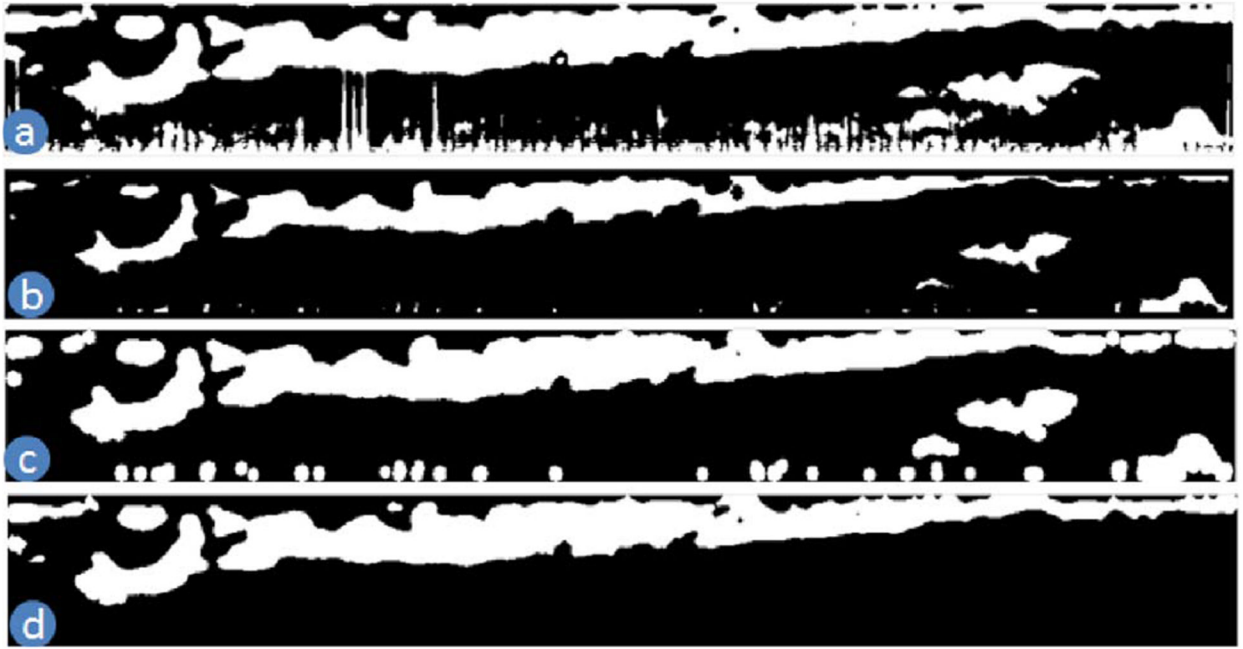


Fig. 6. Vessel pixels after: (a) clustering; (b) morphological operation; (c) morphological closed operation; and (d) applying dynamic distance filter.

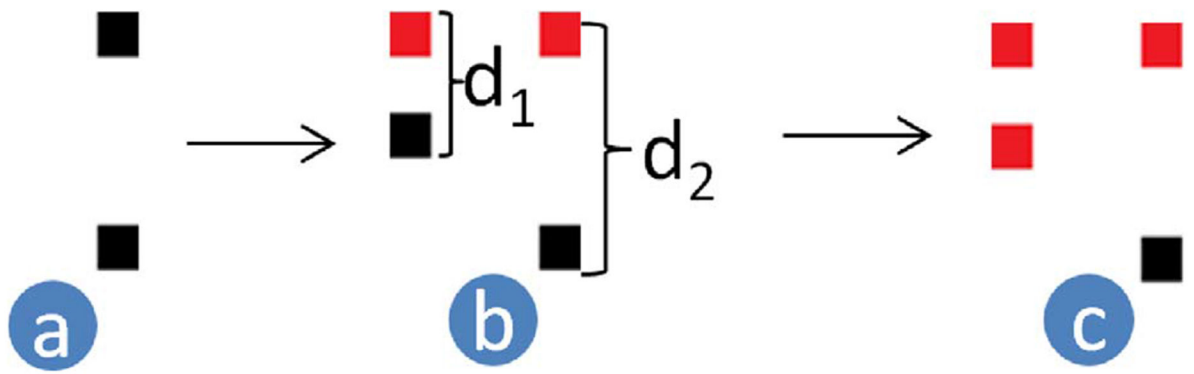


Fig. 7.

(a) Shows black colour pixels found after clustering, red pixels in (b) and (c) are selected as vessel after applying distance filter.

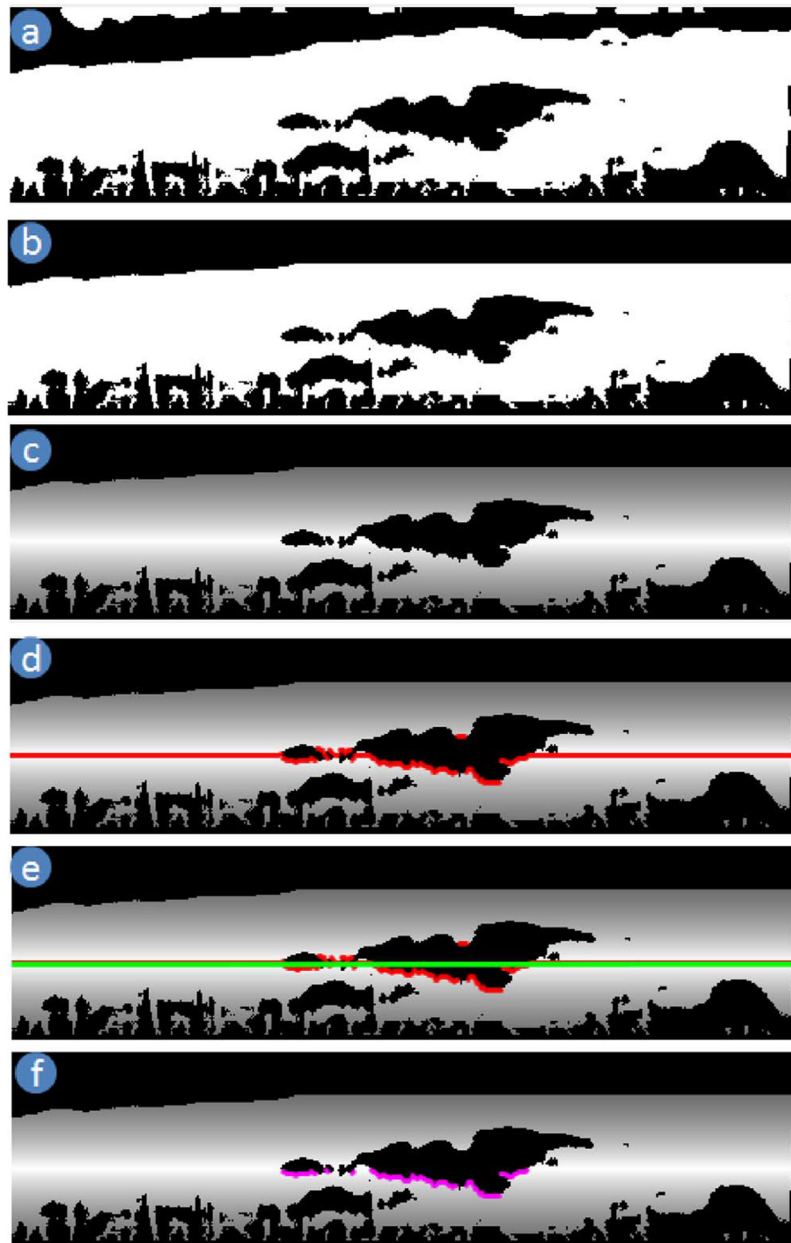


Fig. 8. (a) Surface pixels, (b) following removal of top 100 μm surface pixels, (c) probability map for the surface pixels, (d) candidate pixels (pixels (red) with maximum probability in each A-scan), (e) first order polynomial line on the candidate pixels (green), (f) following removal of candidate pixels (magenta).

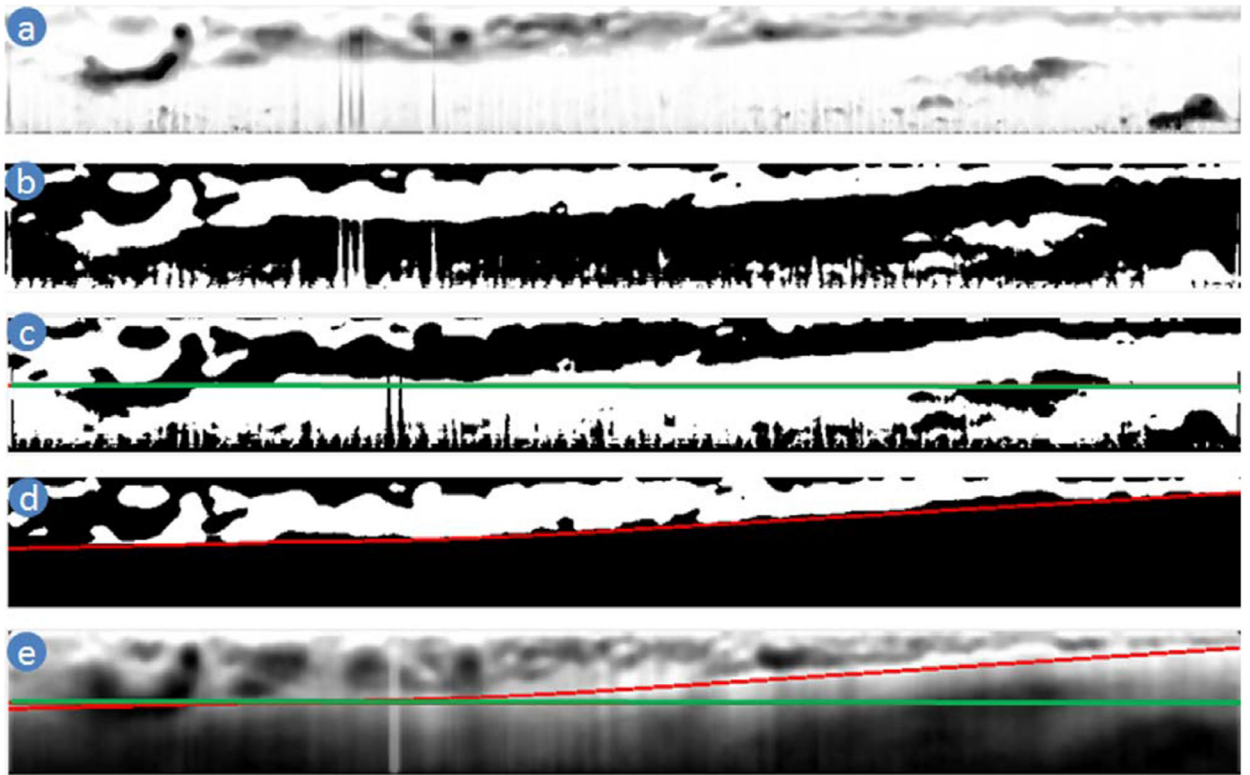


Fig. 9. (a) The DIN image, (b) approximate vessel, (c) approximate CSI (green line) on the surface image (white colour), (d) approximate OCV boundary (red line), (e) approximated CSI (green line) and OCV boundary (red line) on the intensity normalised image.

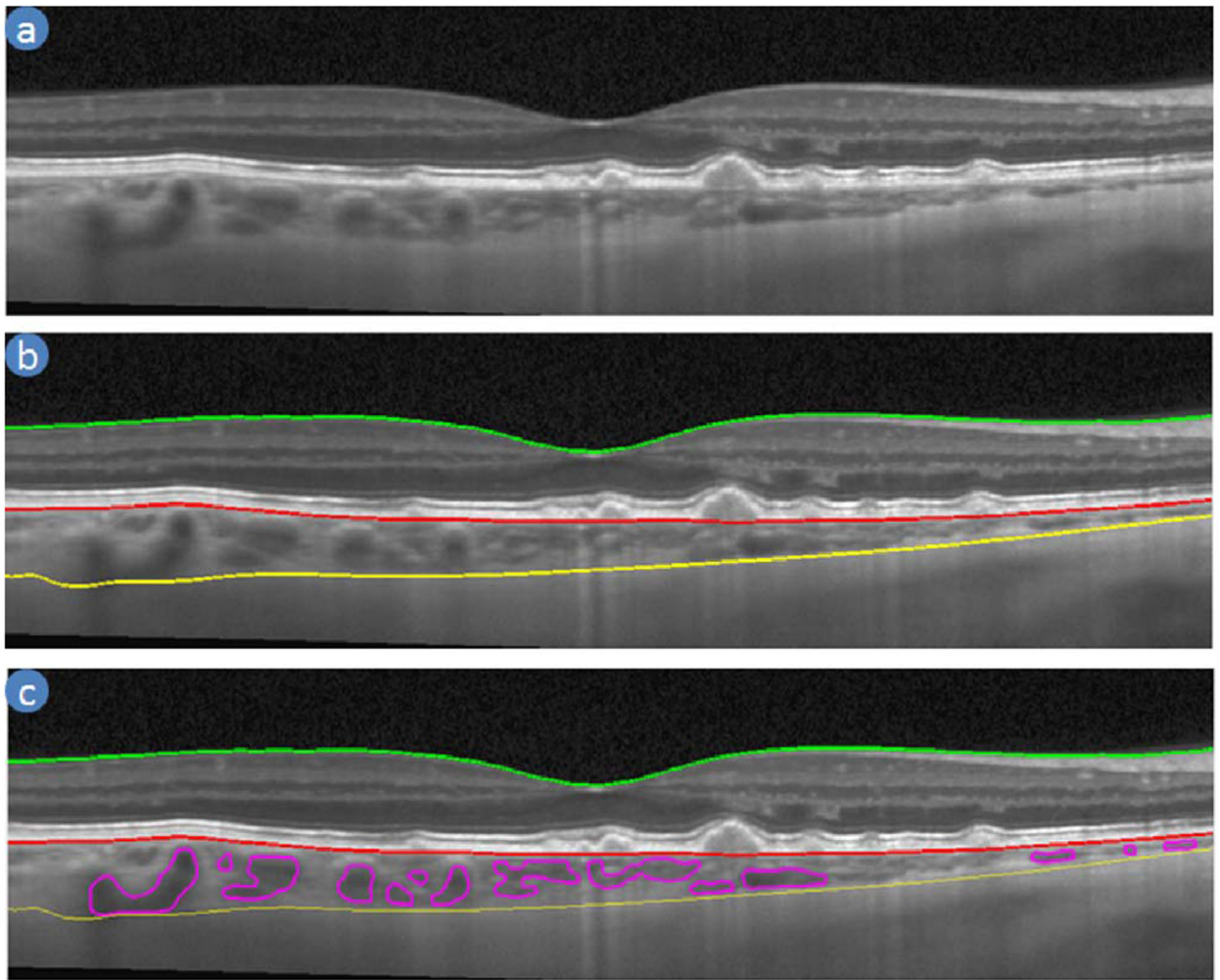


Fig. 10. (a) Original image (b) segmented output of ILM-RNFL (green line), RBC (red line) and CSI (yellow line) (c) segmented output of choroidal vessels (magenta lines).

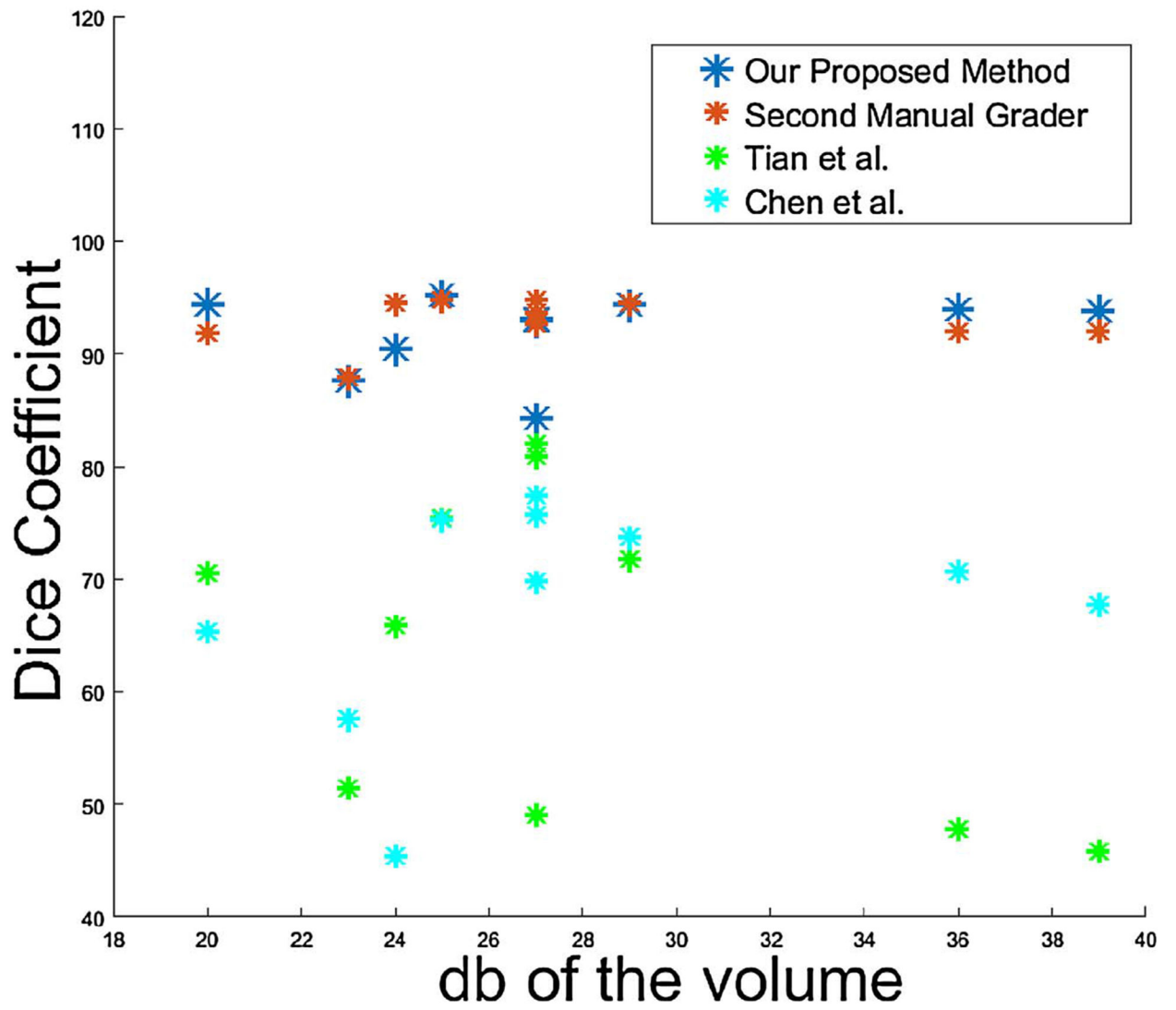


Fig. 11. Dice coefficient against dB of the volume between First Manual Grader and Automatic methods.

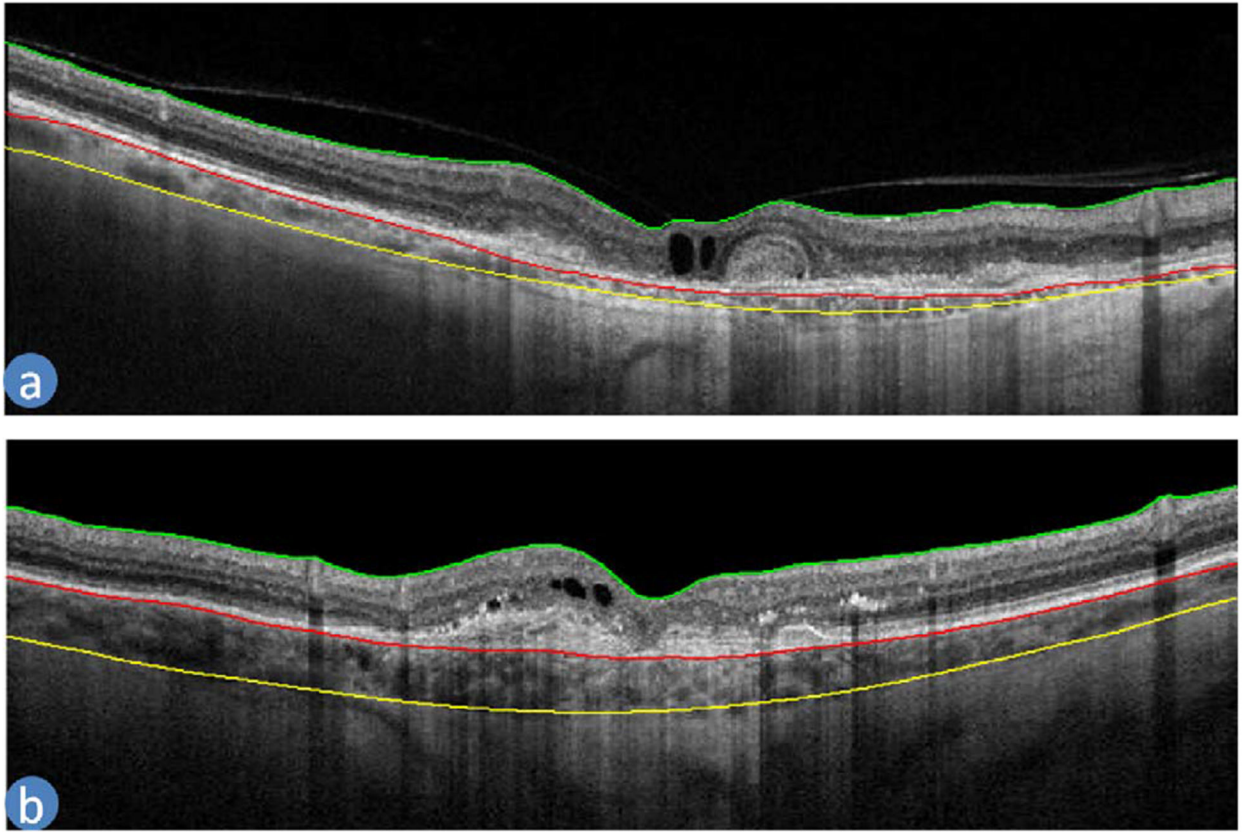


Fig. 12. The output of our proposed method in the SS-OCT retinal scan presented with pathologies.

Table 1

The brief description about available automatic method for the detection of the choroid.

Method	Methodology	Accuracy	Advantage	Limitation/disadvantage
Zhang et al. (2012)	Segmented CV through vesselness map. Multi-scale Hessian matrix and the tensor matrix from SD-OCT images.	Average dice coefficient of the reproducibility is 0.78 ± 0.08 .	Good reproducibility for CV and Cc-equivalent thickness.	Used only healthy subject. Evaluation does not report the boundary positional error.
Kaji et al. (2012)	Segmented the RBC boundary and CSI using Dijkstra shortest path, convex hull, neural network and Active Appearance Model from SD-OCT images.	The average error rate for identifying the CSI is 13%.	High accuracy for boundary detection in the presence of pathology on a large dataset.	Requires large representative training set that includes all possible variations. Method needs 30 s per image.
Torzicky et al. (2012)	Segmented RBC boundary and CSI using a threshold technique based on the degree of polarisation uniformity image and position of the retardation.	A mean repeatability (standard deviation) of thickness measurement of 18.3 μm .	Simple and fast method. Good repeatability for the CTh.	Tested on a small dataset. Accuracy of the boundary segmentation is not analysed. Works only for the (Polarisation sensitive) PS-OCT images.
Duan et al. (2012)	CSI segmented through model analysis, dynamic programming, linear regressions, error detection and correction.	Repeatability error of CTh is 12.55 μm .	Showed high repeatability performance.	Tested on a small dataset. Accuracy of the boundary segmentation is not reported. Works only for the PS-OCT images.
Tian et al. (2013)	BM and CSI segmentation from maximum intensity, gradient, polynomial fitting, and the graph shortest path algorithm from the EDI-OCT images.	The dice coefficient of the choroid is $90.5 \pm 3\%$.	Robust in segmenting the choroid regardless of the imaging modality. Good Dice Coefficient of the choroid.	Largest intensity and gradient based BM detection does not work for pathological states or low quality images (Chen et al., 2015).
Alonso-Caneiro et al. (2013)	RBC boundary and CSI segmentation through edge filter, directional weight, dual brightness probability gradient and the Dijkstra's shortest path algorithm from the EDI-OCT images.	The mean absolute error (MSE) in finding the CSI is 12.72 μm for the paediatric and 16.53 μm for the adults. The MSE of RBC is 2.63 μm .	Evaluated on a large dataset from paediatric and adult populations. High accuracy and repeatability.	Tested only on high-quality dataset.
Yupparaboina et al. (2015)	Segmented RBC and CSI using structural similarity index, tensor voting, and eigenvalue analysis of the Hessian matrix from SD-OCT images.	The MSE, dice coefficient, correlation coefficient and repeatability of the CTh are 9.15 μm , 95.47%, 99.64% and 76.04% respectively.	Evaluated on a large dataset from the adult population. High correlation with manual segmentation. High repeatability for CTh.	Slow method where tensor voting accounts for about 70% of the computation.
Danesh et al. (2014)	Segmented RBC and CSI through dynamic programming, largest gradient, wavelet features and Gaussian mixture model from EDI-OCT images.	The results showed an unsigned error of $9.67 \pm 1.25 \mu\text{m}$ for BM and $38.18 \pm 12.83 \mu\text{m}$ for CSI.	Efficient and accurate method on the good quality images.	Lack of validation for various qualities of images including pathologic states.
Chen et al. (2015)	Segment RBC and CSI through thresholding, gradual intensity distance, graph min-cut-max-flow and the energy minimisation technique from SD-OCT images.	The mean CTh difference and overlap ratio are 6.72 μm and 85.04%, respectively.	Method shown to be superior to method by Tian et al. (Tian et al., 2013).	Not robust, threshold-based BM detection will not work for all dataset of OCT imaging and other pathology existed images.

Table 2

The parameter setting for the equations of the CSI detection.

Eq	Purpose	Parameters	Explanation
8	A probability matrix	$h = 350 \mu\text{m}$ $\eta = 200 \mu\text{m}$	The hypothesis behind computing the probability matrix is that the approximated CSI is more likely to be located near the maximum CTh (350 μm away from the RBC boundary).
9	The distance factor of the approximate CSI	$\alpha = 0.25$ $\beta = 1$ $\delta = 100$	These parameters have been defined empirically that is these configurations give best result for us.
	The distance factor of the approximate OCV	$\alpha = 0.5$ $\beta = 1$ $\delta = 100$	
	The distance factor for normalise intensity of the image	$\alpha = 0.25$ $\beta = 2$ $\delta = 1000$	

The performance of the boundary of RBC and CSI, Choroid and CTh of the Tian et al., Chen et al. and our proposed methods (units in pixel).

Table 3

Evaluation method	Manual segmentation by Grader1 Vs			Manual segmentation by Grader2 Vs			Average manual segmentation Vs				
	Grader2	Tian et al.	Chen et al.	Proposed	Grader1	Tian et al.	Chen et al.	Proposed	Tian et al.	Chen et al.	Proposed
RMSE for RBC	2.60 (1.34)	3.75 (1.79)	2.34 (1.33)	1.91 (1.24)	2.60 (1.34)	3.75 (1.50)	2.83 (1.00)	2.25 (0.89)	3.51 (1.58)	2.43 (0.87)	1.87 (0.75)
RMSE for CSI	7.08 (3.09)	35.45 (12.08)	45.79 (20.13)	8.64 (5.81)	7.08 (3.09)	37.05 (12.36)	43.22 (18.96)	8.68 (6.57)	36.17 (11.97)	44.19 (19.51)	7.71 (6.29)
DC for choroid	92.87%	63.98%	67.87%	92.03%	92.87%	63.10%	69.59%	92.04%	63.62%	68.97%	92.91%
RMSE for CTh	6.90 (2.92)	34.81 (11.56)	46.03 (20.35)	8.79 (5.57)	6.90 (2.92)	35.99 (11.86)	43.96 (19.41)	8.98 (6.21)	35.27 (11.53)	44.85 (19.90)	8.08 (5.89)
r for CTh	0.79	0.5	0.62	0.74	0.79	0.49	0.62	0.71	0.51	0.66	0.76
ICC for CTh	0.76	0.43	0.53	0.69	0.76	0.41	0.54	0.65	0.43	0.56	0.72